

## Externally Fed Star Formation: A Numerical Study

Motahareh Mohammadpour<sup>1</sup> and Steven W. Stahler<sup>2</sup>

Sstahler@astro.berkeley.edu

### ABSTRACT

We investigate, through a series of numerical calculations, the evolution of dense cores that are accreting external gas up to and beyond the point of star formation. Our model clouds are spherical, unmagnetized configurations with fixed outer boundaries, across which gas enters subsonically. When we start with any near-equilibrium state, we find that the cloud’s internal velocity also remains subsonic for an extended period, in agreement with observations. However, the velocity becomes supersonic shortly before the star forms. Consequently, the accretion rate building up the protostar is much greater than the benchmark value  $c_s^3/G$ , where  $c_s$  is the sound speed in the dense core. This accretion spike would generate a higher luminosity than those seen in even the most embedded young stars. Moreover, we find that the region of supersonic infall surrounding the protostar races out to engulf much of the cloud, again in violation of the observations, which show infall to be spatially confined. Similar problematic results have been obtained by all other hydrodynamic simulations to date, regardless of the specific infall geometry or boundary conditions adopted. Low-mass star formation is evidently a quasi-static process, in which cloud gas moves inward subsonically until the birth of the star itself. We speculate that magnetic tension in the cloud’s deep interior helps restrain the infall prior to this event.

*Subject headings:* ISM: clouds, kinematics and dynamics — stars: formation — accretion

### 1. Introduction

We have known for over three decades that low-mass stars form inside the dense cores found throughout larger molecular clouds. Yet the manner in which the cores themselves first arise and then evolve to the point of collapse has eluded understanding. This situation is now changing. A

---

<sup>1</sup>Department of Physics, University of Mazandaran, Babolsar, Iran

<sup>2</sup>Astronomy Department. University of California, Berkeley, CA 94720

growing body of observations, conducted by many researchers, is supplying detailed results that will eventually be the foundation of a much more complete theoretical model.

One key result has been the detection of internal contraction within dense cores. These objects are generally quiescent, with observed molecular line widths that are only marginally broader than thermal (Goodman et al. 1998), at least until the dense core boundary is reached (Pineda et al. 2010). Spectroscopic observations, however, reveal asymmetric emission profiles that signify inward, subsonic motion, even before a star is formed (Lee, Myers, & Tafalla 2001). Among starless cores, which constitute at least half the objects observed (e.g. Forbrich et al. 2009), this so-called “infall signature” is especially common in those with the highest central column density (Gegersen & Evans 2000). Presumably, the latter are more evolved, a supposition bolstered by the observation of systematic trends in chemical abundances (Keto & Caselli 2008).

Even more advanced dense cores, those containing low-mass young stars, also exhibit asymmetric line profiles. The inferred speeds in this case are still subsonic in the outer regions of the cloud, but supersonic within the interior, as one would expect for an object that is undergoing gravitational collapse. Curiously, the spatial extent of supersonic infall is extremely limited, at least in the handful of objects thus far observed with sufficient precision. The spectroscopic studies of Choi et al. (1995), Gegersen et al. (1997), Di Francesco et al. (2001), and Belloche et al. (2002) find that the sonic transition occurs only 0.01 - 0.02 pc from the protostar, in a dense core of linear size 0.1 pc. Submillimeter observations of dust continuum emission reach a similar conclusion via a different route. Shirley, Evans, & Rawlings (2002) show that collapse cannot pervade the interior of the core, as it would alter the density profile in a manner that is not observed.

This finding of spatially confined infall is sharply at odds with conventional theory. In the still widely used self-similar model of Shu (1977), the infall region spreads outward as a rarefaction wave traveling at the ambient sound speed  $c_s$ . Just inside the wavefront, at  $r = r_f = c_s t$ , the infall speed is zero, and becomes supersonic at  $r \simeq 0.4 r_f$ .<sup>1</sup> By the time the protostar’s mass becomes half that of the parent cloud, the rarefaction wave has already reached the cloud boundary. The large number of simulations that followed Shu’s semi-analytic treatment paint a similar picture (Foster & Chevalier 1993; Ogino, Tomisaka, & Nakamura 1999; Motoyama & Yoshida 2003; Aikawa et al. 2005).

Another departure between theory and observation is embodied in the venerable “luminosity problem.” The luminosity of a protostar is supplied by mass accretion onto its surface, and is in fact proportional to  $\dot{m}_*$ , the instantaneous mass accretion rate. Kenyon et al. (1990) first noted that the  $\dot{m}_*$  given by theory yields a luminosity greater by an order of magnitude than those observed in the most deeply embedded infrared and submillimeter sources. In the model of Shu (1977),  $\dot{m}_* = m_o c_s^3 / G$ , where  $m_o$  is a numerical factor close to unity. In numerical simulations,  $\dot{m}_*$  varies in

---

<sup>1</sup>Choi et al. (1995) and Gegersen et al. (1997) quote values of  $r_f$  obtained by matching their data to the model of Shu (1977). We further used this model to infer the radius of the sonic transition.

time, but is generally even larger, exacerbating the discrepancy (e.g. Ogino, Tomisaka, & Nakamura 1999, Fig. 7).<sup>2</sup>

Solving both these problems, which are almost certainly related, will require an improved model of cloud collapse. The infall signature observed in starless cores can sometimes be detected far outside the densest gas (Lee, Myers, & Tafalla 2001). That is, a subsonic inward drift is superposed on the turbulent gas surrounding the core. In some cases, inward contraction is seen throughout an entire, cluster-forming cloud (Walsh, Bourke, & Myers 2006). These observations support the entirely reasonable view that there is no physical barrier between a dense core and its external medium. Thus, the inward creep of gas that forms the object should continue unabated through the point of star formation.

In conventional simulations, however, the core boundary is characterized by zero inward velocity. Thus, the initial mass of the dense core is never replenished, but steadily drains onto the protostar, at least until a stellar wind disrupts the cloud and ends accretion. More realistically, the core boundary should be *open*. Matter drifts across this boundary continually, replenishing in part the mass being lost to the central star. The actual drift speed is subsonic, as indicated by the spectroscopic studies mentioned earlier.

Theorists have begun to consider modified collapse models that incorporate an open boundary. Gong & Ostriker (2009, 2011) simulated dense core formation out of a converging flow (spherical or plane-parallel). A dense, hydrostatic object grows and then eventually collapses to form a central star. The model core in this case indeed had an open boundary, but Gong & Ostriker chose the infall speed to be supersonic, more characteristic of the inferred *random* speeds in background gas than the systematic, inward *drift* speed. Their dense core thus formed inside a shock front, and was supersonically collapsing as a whole even before the star formed. This prediction is not in accord with the velocity distribution inferred from spectroscopy.

Dalba & Stahler (2012) explored a spherical, open-boundary model, in which gas enters subsonically. For simplicity, they removed the dense core boundary to infinity, i.e., to a radius much greater than the accretion value,  $2G M_*/c_s^2$ , where  $M_*$  is the (changing) protostar mass. They also assumed that  $M_*$  increases through a steady-state flow, in which the mass transport rates across all spherical shells surrounding the star are identical and equal to  $\dot{m}_*$ . Within this context, the results were encouraging. The actual value of the accretion rate is reduced from  $c_s^3/G$  by a factor of  $2\beta$ , where  $\beta$  is the incoming Mach number. The sonic point, marking the boundary of true infall onto the star, spreads outward subsonically, at speed  $\beta c_s$ . Both findings are closer to what is observed.

In this contribution, we use numerical simulations to treat fully time-dependent collapse with

---

<sup>2</sup>Some recent simulations find that infalling gas landing on the protostellar disk is stored for many orbital periods, and released onto the star in episodic bursts. Thus, the luminosity problem is ostensibly averted, at least in between bursts (see Vorobyov & Basu 2010, and references therein). For computational convenience, these simulations treat the entire dense core as a thin disk, and so cannot address the issue of cloud infall.

an open boundary, still within the framework of a spherically symmetric flow. We endow the dense core with a finite radius, whose value is taken from observations. Recent, far-infrared imaging by the Herschel satellite finds that dense cores tend to be nested inside narrow filaments within the larger parent cloud (Molinari et al. 2010). Orthogonal to the filaments are fainter striations that are roughly parallel to the ambient magnetic field (Palmeirim et al. 2012). Gas may be flowing along the striations to join onto the filament.

The main filaments imaged by Herschel have lengths of several parsecs and strikingly similar diameters of about 0.1 pc (Arzoumian et al. 2011). This figure matches the long-known diameters of dense cores (Jijina, Myers, & Adams 1999). It is becoming clear that the size of a dense core is predetermined, i.e., the object forms by gas drifting into, and perhaps also along, a filament of fixed diameter. In our simulations, we have taken the outer boundary of the flow to be a sphere that is 0.1 pc in diameter.

The new simulations corroborate, but only in part, the previous results from the steady-state model. We find again that the sonic point spreads slowly and that  $\dot{m}_*$  falls appropriately below  $c_s^3/G$ . However, there is an early, transient stage of the inflow, during which  $\dot{m}_*$  is much *greater* than  $c_s^3/G$ . During this “accretion spike,” the sonic point races out at a speed higher than  $c_s$ . Although the duration of the accretion spike is relatively brief,  $\dot{m}_*$  is so high that the protostar gains essentially all of its mass under these conditions. Moreover, supersonic infall engulfs most of the dense core during the period of the spike. Thus, this model too is at odds with the observational facts. The idea of externally fed star formation remains well motivated, but the actual flow creating the protostar must be subsonic. It seems impossible to accomplish this feat in a purely hydrodynamic scenario. That is, magnetic support must play a key role during dense core contraction.

In Section 2 below, we present our method of solution, including the manner in which we choose the initial state of the dense core. Section 3 gives numerical results for the collapse, focusing on the critical evolution of the mass accretion rate and of the sonic point. Finally, Section 4 places our findings in context, and suggests fruitful directions for future investigations.

## 2. Solution Strategy

### 2.1. Numerical Method

Following many previous researchers, we idealize the flow building up the dense core to be spherically symmetric. Real dense cores are not spheres, but have projected aspect ratios of about 2:1 (e.g. Ryden 1996). It is an open question whether the observed core shapes result from *internal* magnetic support, which is inherently anisotropic, or from *external* influences, such as pressure gradients across the bounding filaments. By restricting ourselves to a spherical inflow, we are implicitly discounting all forces but those associated with thermal pressure and self-gravity. This is a reasonable first approximation, given the narrow observed linewidths of tracer molecules. To

the extent that our model fails to match observations, additional forces must be considered.

We take the gas to be isothermal, both spatially and temporally, with a sound speed of  $c_s = 0.2 \text{ km s}^{-1}$ . Within a molecular cloud, this speed corresponds to a gas kinetic temperature of 12 K, which is representative of observed values for starless cores (Jijina, Myers, & Adams 1999). Thus far, our assumptions are standard ones. Our main innovation is to apply an open outer boundary condition. We establish the core boundary at a radius of  $r = r_b$ , taken to be 0.05 pc. Gas drifts across this boundary at the fixed speed  $v_b$ , assumed here to be  $0.2 c_s$ , in accord with spectroscopic observations of the infall signature (Lee, Myers, & Tafalla 2001). This accreting gas has a fixed density throughout the calculation, which we set to establish continuity with the initial state, as described below. We thus maintain a constant external rate in each evolutionary run,  $\dot{m}_{\text{ext}} = 4 \pi r_b^2 \rho_b v_b$ .

In all our simulations, we have employed the publicly available code ZEUS-MP (Hayes et al. 2006). We covered the flow with 350 zones, logarithmically spaced to give finer resolution of the central region. At  $r = r_b$ , we applied the inflow boundary condition, which allowed us to fix the outer velocity and density. At  $r = 0$ , we applied the reflecting boundary condition, forcing the velocity to vanish at the origin.

Once the central density climbed to  $6 \times 10^{-14} \text{ gm cm}^{-3}$ , some five orders of magnitude higher than its initial value, we inserted a central sink cell, following the technique of Boss & Black (1982). This event signaled the formation of the protostar. We initially chose the radius for the sink cell so that the density dropped by a factor of 4 from the center to its edge, and then maintained that radius thereafter. In practice, the sink cell covered about 8 zones. At the edge of the cell, we applied the outflow boundary condition. We also calculated the stellar accretion rate  $\dot{m}_*$  at that point.

## 2.2. Choice of Initial State

To see how a spherical dense core evolves while undergoing steady, subsonic accretion, we have explored a broad range of initial states. In all cases, we began with a linear velocity profile. That is, the initial velocity  $v_0(r)$ , taken to be positive for inflow, was chosen to be

$$v_0 = v_b r / r_b . \quad (1)$$

By adopting this profile, we ensured that the subsequent accrual of mass through the boundary occurred smoothly, with no artificial pileup or deficit in gas at  $r = r_b$ .

Each evolutionary run is then characterized by the starting density profile,  $\rho_0(r)$ . Table 1 lists all our runs, with the leftmost column giving the initial density contrast from center to edge,  $\rho_c / \rho_b$ . In the first two runs, we adopted a uniform initial density. Thus,  $\rho_c / \rho_b$  is unity in these cases. This imposed condition is, of course, highly artificial astrophysically, and was chosen to compare our

results with earlier collapse studies. Thus, we retained a closed boundary condition ( $v_b = 0$ ) in the first run, and switched over to our standard open boundary, with  $v_b = 0.2 c_s$ , for the second.

In all our subsequent simulations, listed below the horizontal line in the table, we used an open boundary condition and an initial cloud that was in force balance between self-gravity and thermal pressure. That is,  $\rho_0(r)$  corresponded to the profile of an equilibrium, isothermal sphere. As is well known, these equilibria comprise a one-parameter family. For each run, we fixed the density contrast  $\rho_c/\rho_b$ , and then used a numerical solution of the isothermal Lane-Emden equation to find the density profile. We obtained the dimensional density  $\rho(r)$  by requiring that the outer boundary be located at  $r = r_b$ , where  $r_b$  was fixed at 0.05 pc.

An equilibrium starting state is assuredly more realistic than a uniform-density one, which is out of force balance. Nevertheless, observations give little clue as to the appropriate initial configuration, which is therefore rather arbitrary in the simulations. We tested a broad range of states, corresponding to both stable and unstable equilibria. That is, some initial states had  $\rho_c/\rho_b$  below the critical, Bonnor-Ebert value of 14.0, while others had higher values. For our lowest density contrast, we set  $\rho_c/\rho_b = 1.45$ . Here, the cloud mass was  $0.31 M_\odot$ , and the number density in hydrogen molecules was  $1 \times 10^4 \text{ cm}^{-3}$ . This cloud would be marginally detectable using a tracer molecule such as  $\text{NH}_3$ .

As we evolved each cloud, gas flowed across the boundary at the speed of  $v_s = 0.2 c_s$  and a fixed density of  $\rho_b$ . For continuity, we chose the latter to be the outermost density in the initial state. Thus, the externally imposed accretion rate  $\dot{m}_{\text{ext}}$  varied from one run to another, though not by a large amount. The fifth column in the table gives the actual values of  $\dot{m}_{\text{ext}}$  in units of  $c_s^3/G$ . Notice that  $\dot{m}_{\text{ext}}$  is less than  $c_s^3/G$  in every case, in accordance with the earlier analysis of Dalba & Stahler (2012).

### 3. Results

#### 3.1. Uniform-Density Initial States

##### 3.1.1. Closed Boundary

By choosing a uniform-density initial state and setting the boundary velocity  $v_b$  to zero at all times, we are essentially repeating the classic study of Larson (1969). Comparison of our results with Larson’s served both to validate our numerical method and to identify the changes effected by subsequently employing an open boundary. We chose the initial density  $\rho_0$  to be the minimum required for the cloud to undergo collapse. We found this minimum density to be  $\rho_0 = 1.40 \times 10^{-19} \text{ gm cm}^{-3}$ , corresponding to a cloud mass of  $1.08 M_\odot$ . Using the conventional definition of free-fall time,

$$t_{\text{ff}} \equiv \sqrt{\frac{3\pi}{32G\rho_0}}, \quad (2)$$

our initial state had  $t_{\text{ff}} = 1.78 \times 10^6$  yr. Larson (1969) adopted the slightly larger  $r_b$ -value of 0.053 pc, and used a correspondingly lower  $\rho_0$  of  $1.10 \times 10^{-19}$  gm cm $^{-3}$ .

By design, the central density of the cloud monotonically increased with time. However, the internal velocity did not develop smoothly from the initial linear profile. As long as the velocity was everywhere subsonic, the profile changed in an erratic manner. Gas did not simply come to rest at the origin, but underwent a bounce, temporarily creating a central region of outwardly moving material. This reversal, in turn led to irregularities in the evolving density profile. At the time  $t_s$  listed in the table, the peak inward velocity was supersonic. After that point, both the velocity and density profiles became smooth.<sup>3</sup>

The left panel of Figure 1 shows the evolution of the density profile. The solid curves show the rise in density prior to  $t_*$ , the time at which the protostar forms, according to the criterion previously described. In the outer region of the cloud, the density quickly develops an  $r^{-2}$  profile, and flattens toward the center. These results qualitatively match those described by Larson (1969) and displayed in his Figure 1. In Larson’s simulation, the star formed  $4 \times 10^5$  yr after the initiation of collapse, while our corresponding time was closer to  $3 \times 10^5$  yr (see Table 1). This difference stems from our choice of a slightly higher initial density.

Following the formation of the protostar, the surrounding gas eventually enters into a state of free-fall collapse. The mass transfer rate across each spherical shell is about the same, and  $\rho(r)$  attains a flatter,  $r^{-3/2}$  profile.<sup>4</sup> As cloud mass drains onto the central star, the free-fall speed at any radius increases and the overall magnitude of the density declines. These later density profiles are displayed as dashed curves in the left panel of Figure 1. Once again, the same results are well described by Larson (1969) and subsequent authors.

The fact that the peak interior velocity becomes supersonic prior to the formation of the star has an important consequence. In Figure 2, we show the evolution of  $\dot{m}_*$ , the mass accretion rate onto the star. This rate is, of course, only defined for  $t \geq t_*$ , and has been set to zero before that time. Shortly after this time,  $\dot{m}_*$  is very large relative to the canonical value  $c_s^3/G$ , exceeding it by a factor of 20. The rate then drops in a relatively brief time. The star thus undergoes an initial “accretion spike,” caused by the buildup of supersonic speeds in the dense core prior to the formation time  $t_*$ .

To understand further the physical basis of this phenomenon, we have run comparison simulations in which  $\dot{m}_*$  was calculated from  $t = 0$ . For  $t < t_*$ , we used the mass transport rate across what later became the outer boundary of the sink cell. The resulting curves were indistinguishable from those in Figure 2. Thus, the sharp rise in the accretion spike is independent of the precise

---

<sup>3</sup>The transient irregularities described here did not occur if we used an initial density substantially higher than the minimum value required for collapse.

<sup>4</sup>It is this flattening of the density profile that is *not* detected throughout the bulk of observed dense cores containing stars (Shirley, Evans, & Rawlings 2002).

definition of  $t_*$ .

The amount of mass accumulated during the accretion spike is not small, as we now quantify. Observational comparison of the mass distributions of dense cores with those of newly formed stars (the initial mass function) shows that, on average, a dense core produces a star containing about 0.3 times the core mass (Alves, Lombardi, & Lada 2007; Rathborne et al. 2009). Accordingly, we let  $t_f$  be the time in our simulations when the protostar is likely to build up its final mass, which we set to 0.3 times the current cloud mass. This time is given in the fourth column of the table. For the specific case at hand, we see that  $t_f$  exceeds  $t_*$  by a relatively small amount, about  $2 \times 10^4$  yr.

The time  $t_f$  is also shown by a filled circle in Figure 2. We see vividly that this time occurs before  $\dot{m}_*$  has declined to a value of  $c_s^3/G$  or less. In other words, *most of the stellar mass accumulates while the accretion rate is still large*. This result, as we shall see, is quite general. In the present case, the average accretion rate from time  $t_*$  to  $t_f$  is about  $8c_s^3/G$ . This average rate, symbolized as  $\langle \dot{m}_* \rangle$ , is given for all simulations as the sixth column in the table. To understand fully the physical character of the collapse, we have allowed this and subsequent simulations to run well past  $t = t_f$ , although the star would in fact have dispersed the dense core soon after this point.

Another quantity that we can compare with observations is the sonic point  $r_s$ , defined as the outermost radius at which the incoming fluid speed matches  $c_s$ . As the collapse proceeds and the gas velocity generally increases,  $r_s$  moves outward. Figure 3 shows the advance of  $r_s$  in the first simulation. At  $t = t_s$ , the sonic point is located at  $0.14r_b$ . It first races outward at supersonic speed. We denote this initial speed as  $(\dot{r}_s)_0$  and list it in the last column of the table. Although its outward advance slows with time, the sonic point is still traveling at  $1.03c_s$  at the time  $t_f$ , again shown by the filled circle in the figure. At this point,  $r_s$  has covered a radius of about  $0.3r_b$ . By the last time shown in Figure 3, the speed of the sonic point has declined to  $0.08c_s$ . The mass of the cloud has fallen to 0.08 times its initial value.

### 3.1.2. Open Boundary

Our next initial state was again of uniform density, and with the same  $\rho_0$ -value. This time, however, we applied the more realistic open boundary condition at the cloud edge. The righthand panel of Figure 1 shows that the density profiles evolve in a qualitatively similar manner as for the closed boundary. Prior to the formation of the central star, which now occurs at the earlier time of  $t_* = 1.86 \times 10^5$  yr, each profile again consists of an  $r^{-2}$  envelope and a relatively shallow central core. After the star forms, the density attains the  $r^{-3/2}$  slope characteristic of steady, free-fall collapse. In this case, the cloud mass never vanishes, and it takes longer for the stellar mass to overtake it. Hence, it also takes longer for the infall speed to approach true free-fall, and the density profiles accordingly evolve more slowly.

The profiles in Figure 1 have one curious feature that calls for explanation. Although gas flows



across the boundary with a fixed density, the figure shows that  $\rho(r)$  just inward of that point falls sharply before starting its more gradual, inward rise. This sudden drop in density, typically by a factor of 2, is accompanied by a corresponding increase of the velocity. Gravity is pulling gas inward faster than it can be supplied from the outside, creating a partial vacuum. This phenomenon is unphysical, an artifact of our fixing the drift speed at  $0.2 c_s$ . Since the exterior mass accretion rate is not effected, there is no impact on the collapse process. In any event, we shall later see that the same phenomenon occurs, albeit to a lesser extent, when we begin with states near hydrostatic equilibrium.

Returning to Figure 2, which shows the evolution of  $\dot{m}_*$ , we see first that formation of the star occurs earlier when we use an open boundary. The reason is simply that more cloud mass is available to accumulate at the origin. As before, the internal velocities become supersonic, and  $\dot{m}_*(t)$  exhibits a sharp initial spike. From the location of the filled circle, marking the time  $t_f$ , we again see that the bulk of the protostar’s mass is gained while the accretion rate is still relatively high. According to Table 1, the average rate building up the protostar is  $10.9 c_s^3/G$ . In this case,  $\dot{m}_*(t)$  does not asymptotically vanish, as it did for the closed boundary, but levels off at the externally imposed value,  $\dot{m}_{\text{ext}} = 0.84 c_s^3/G$ , as also listed in the table.

Finally, Figure 3 shows that the sonic point starts at a much larger radius ( $0.54 r_b$ ) than in the closed boundary case ( $0.14 r_b$ ). That is, more of the cloud is collapsing supersonically at the point of star formation. The initial speed of the sonic point,  $(\dot{r}_s)_0$ , is again quite high, almost  $2 c_s$ . At  $t = t_f$ ,  $r_s$  covers 0.64 of the full cloud radius. The point comes close to the cloud boundary by  $t = 3 \times 10^6$  yr, and thereafter remains nearly static. That is, almost the entire cloud is collapsing supersonically at this late epoch, despite the continuing, subsonic injection speed.

## 3.2. Equilibrium Initial States

### 3.2.1. Density and Velocity Evolution

We next began with configurations that are in a state close to hydrostatic balance. As before, the density profiles did correspond precisely to equilibria. Since each cloud had a non-zero velocity profile from the star, given by equation (1), it was actually in a near-equilibrium state that evolved quasi-statically, at least early in the simulation.

When we started with our minimal, center-to-edge density contrast of  $\rho_c/\rho_b = 1.45$ , we found that the cloud not only evolved through all the stable equilibria in the isothermal sequence ( $\rho_c/\rho_b < 14.0$ ), but beyond this point into the regime of unstable states. When the central density climbed to  $4 \times 10^3$  times the edge value, the peak inward velocity became supersonic. This event occurred at  $t_s = 1.54 \times 10^6$  yr. A short time later, at  $t_* = 1.55 \times 10^6$  yr, the central star formed, and both the density and velocity increasingly resembled those corresponding to free-fall collapse onto the central mass.

The sequence of events was qualitatively the same when we started with configurations having a larger density contrast. Figure 4 shows the evolution of the density for the last stable starting state, that with  $\rho_c/\rho_b = 14.0$ . In the purely hydrodynamic, spherical model assumed here, this configuration is the most realistic starting state, as recognized by many others (Hunter 1977; Foster & Chevalier 1993; Ogino, Tomisaka, & Nakamura 1999; Aikawa et al. 2005). However, previous authors increased the initial density everywhere above the equilibrium value to ensure that the system evolved with time. We do not require this artifice, as the continual addition of mass from the outside naturally drives the cloud into collapse.

Figure 4 shows vividly how the central density shoots up before the internal velocity becomes supersonic at  $t_s = 2.52 \times 10^5$  yr. The dashed curve is the profile at  $t = 3.0 \times 10^5$  yr, after the point of star formation,  $t_* = 2.59 \times 10^5$  yr. Already at this time, the density is everywhere diminishing, as the cloud enters a state of free fall onto the growing protostar.

The evolution of the internal velocity profile, for the same starting state, is displayed in Figure 5. Here, the times are the same as in the preceding plot. As long as the velocity is wholly subsonic, its peak position moves steadily inward. As we have seen, the peak velocity becomes supersonic shortly before the star forms. From the shape of the velocity profile, it is clear that there are *two* sonic points just after  $t_s$ . The inner one vanishes once the star forms and the flow assumes the typical free-fall profile. In all plots of  $r_s$ , we only display the outer point. Note also that the time  $t_s$  when the flow becomes supersonic is 3.45 times the cloud’s free-fall time, based on its initial central density. Stahler & Yen (2009), who tracked the cloud evolution from the same starting state via perturbation theory, reached a similar conclusion. Both results indicate that a starless core can contract subsonically for a relatively long time before entering into a state of true collapse.

Two final remarks are in order. First, Figure 5 shows that the velocity rises quickly above its imposed boundary value just inside of  $r_b$ . This rise corresponds to the drop in outer density mentioned earlier, and occurs here for the same reason. Lastly, we see that no shock arises in the flow during the time interval from  $t_s$  to  $t_*$ , when the velocity peaks at a supersonic value and then plunges inward. The reason is that even the supersonic gas is moving rapidly enough that it cannot be overtaken by the more rapidly moving gas outside it.

### 3.2.2. Mass Evolution

Figure 6 shows the evolution of the stellar accretion rate  $\dot{m}_*$ , both for the initial equilibrium state with  $\rho_c/\rho_b = 1.45$  and for that with  $\rho_c/\rho_b = 14.0$ . Not surprisingly, the star forms more quickly when the initial density contrast in the cloud is greater. In both cases, there is a sharp accretion spike caused by the buildup of supersonic velocities at early times. The total mass of the star is again accumulated while  $\dot{m}_*$  is relatively high, as indicated by the filled circles in the figure. According to the table, the average  $\dot{m}_*$  during the epoch of star formation varies between 10 and

11 times  $c_s^3/G$  for all density contrasts of the parent cloud. The accretion rate does not decline to zero at long times, as in the closed-boundary simulation, but approaches the externally imposed value. All these external values fall below  $c_s^3/G$ , as listed in the table.

Figure 7 shows directly the evolution of the both the cloud and stellar mass, again for initial density contrasts of  $\rho_c/\rho_b = 1.45$  and 14.0. Before the point of star formation, the cloud mass (*dashed curve*) climbs linearly with time, in accordance with the constant external mass accretion rate being imposed. Just at  $t = t_*$ , this mass falls sharply. The stellar mass (*solid curve*) climbs quickly during the accretion spike, then settles to the slower rate corresponding to  $\dot{m}_{\text{ext}}$ .

The filled circles in Figure 7 show how quickly the full stellar mass is attained. From Table 1, the interval over which the star builds up,  $t_f - t_*$ , first *decreases* with higher initial density contrast, then *increases*. The minimum time interval occurs for an initial density contrast near  $\rho_c/\rho_b = 8$ . Not coincidentally, this configuration has the highest average accretion rate,  $\langle \dot{m}_* \rangle$ , of all those we considered. In any event,  $t_f - t_*$  is always a small fraction, typically 10 percent, of the cloud’s initial free-fall time.

The interval  $t - t_*$  is a similarly small fraction of the total time elapsed since subsonic infall begin. Although we do not trace the evolution prior to this point, our results imply that only a small fraction of dense cores should contain protostars. And yet the observed numbers of starred and starless cores are comparable (e.g. Jessop & Ward-Thompson 2000). Some of these objects might not be true protostars, but more mature, pre-main-sequence stars that have not yet fully dispersed their parent dense cores. Additionally, there is undoubtedly an observational bias toward observing cores of higher column density and density contrast (see also Gong & Ostriker 2009, who emphasize this point).

### 3.2.3. Sonic Point

We display in Figure 8 the evolution of the sonic point  $r_s$  over the full range of initial density contrasts. In all cases, this point first appears well outside the star. Its initial speed of advance, listed as  $(\dot{r}_s)_0$  in the table, is always highly supersonic. The speed thereafter generally declines. For relatively low initial density contrast, the point advances faster as we consider denser initial states. This trend reverses at  $\rho_c/\rho_b \sim 8$ . For even higher initial density contrast,  $r_s$  starts out progressively closer to the star and does not advance as far in a given time.

In all our simulations, the trajectories  $r_s(t)$  are remarkably similar. Figure 9 highlights this point. Here, we have overlaid all the curves from Figure 8, shifting the vertical axis so that the sonic point always starts in the same position. While there are detailed differences from case to case, the same pattern recurs – an early advance in  $r_s$ , followed by a longer expansion at slower speed. It is also generally true that  $r_s$  spans a large fraction of the full cloud radius at  $t = t_f$ , when the star has accumulated most of its mass. Typically,  $r_s/r_b = 0.3 - 0.5$  at this point. For the most realistic starting state, that with  $\rho_c/\rho_b = 14.0$ , this ratio is  $r_s/r_b = 0.45$ .

The state with the largest initial density contrast,  $\rho_c/\rho_b = 100$ , represents a highly unstable configuration, and is not a realistic candidate model for a starless core. Indeed, the density profile approximates that of the singular isothermal sphere, whose collapse was studied by a number of investigators (Larson 1969; Penston 1969; Shu 1977; Hunter 1977; Whitworth & Summers 1985). All these researchers focused on *self-similar* collapse, a process that could occur, at least in principle, if the cloud’s bounding surface were removed to infinity. On the other hand, Dalba & Stahler (2012) studied the *steady-state* collapse of the singular configuration, in which the cloud is being fed by an external flow with subsonic speed  $\beta c_s$ , where  $\beta < 1$ . In contrast to the self-similar studies, they found that the sonic point advances slowly, also at a speed of  $\beta c_s$ , while  $\dot{m}_*$  is a constant, given by  $2\beta c_s^3/G$ .

In our fully time-dependent simulation of the  $\rho_c/\rho_b = 100$  state, both predictions of Dalba & Stahler (2012) are borne out, but only after initial transients have died away. According to Table 1, the sonic point first races out supersonically, as in all other simulations. Eventually, the speed of this point does decline to the expected subsonic value, but only long after the time  $t_f$ . Figure 10 shows that  $\dot{m}_*(t)$  follows a similar route. We first see the usual accretion spike at  $t = t_*$ . Thereafter, the accretion rate does asymptotically approach the predicted value of  $2\beta c_s^3/G = 0.40 c_s^3/G$ . The growth of the stellar mass itself, shown in Figure 10 as the dashed curve, thus slows down over this long epoch. Once again, the observationally relevant stellar mass is built up much earlier, during the early decline of the spike. The average accretion rate during this period thus has the relatively high value of  $\langle \dot{m}_* \rangle = 8.20 c_s^3/G$ .

## 4. Discussion

### 4.1. Onset of Collapse

The results of this study bear not only on star formation per se, but also on the more general issue of starless core dynamics. As mentioned earlier, the denser subclass of these clouds exhibits spectroscopic signs of slow contraction. The origin of this contraction is still uncertain. Most researchers have concluded that ambipolar diffusion of the cloud’s internal magnetic field is too slow a process (e.g. Lee & Myers 2011). To be sure, model results are sensitive to the assumed cloud geometry and initial mass-loading of the magnetic field lines (Tassis et al. 2012). Ambipolar diffusion is also enhanced, at least in principle, through turbulence (Fatuzzo & Adams 2002), but dense cores are noted for their quiescent interiors. All told, this mechanism does not seem promising.

Since the inward motion appears only in the starless cores of highest density, self-gravity must be its main driver, whether or not a magnetic field is present. To illustrate this point, Stahler & Yen (2009, 2010) reproduced the observed velocity profiles using a non-magnetic, spherical cloud with the marginally stable density contrast of  $\rho_c/\rho_b = 14.0$ . In their model, contraction is due to non-linear growth of the cloud’s fundamental oscillation mode, which has zero frequency to linear order. One noteworthy finding was that this period of contraction is relatively protracted, typically lasting

about 4 times the cloud’s free-fall time, based on its initial central density. Thus, the relatively high fraction of starless cores also finds a natural explanation.

Our current simulation corroborates these results. For a cloud with the density contrast in question, the internal velocity is appropriately subsonic for a relatively long period, and does not become supersonic until  $2.52 \times 10^5 \text{ yr} = 3.45 t_{\text{ff}}$  after the start of the evolution. This continued agreement with the spectroscopic studies, together with the proliferating observations of the immediate dense core environment, reinforce our belief that the contraction represents the approach to collapse of a cloud that has been driven to a marginally stable state through external accretion of gas.

## 4.2. Accretion Spike

On the other hand, the conundrum known as the luminosity problem remains. We find that, following the slow contraction phase, supersonic velocities arise throughout the interior portion of the cloud. This fast, incoming material creates a sudden burst of accretion at the onset of star formation. The accretion spike lasts less than a free-fall time, but long enough to build up essentially all of the protostar’s mass. It is only long *after* this point, when a real dense core would have already been dispersed by a stellar wind, that  $\dot{m}_*$  declines to the relatively slow rate found by Dalba & Stahler (2012) for a cloud undergoing steady, external accretion.

The accretion spike occurs in theoretical models regardless of the specific boundary conditions adopted. Thus, Foster & Chevalier (1993) posited a spherical cloud of constant mass, whose boundary was held at fixed pressure. Their cloud radius, unlike ours, shrank during the evolution. Starting with the density contrast  $\rho_c/\rho_b = 14.0$ , they found that 44% of the cloud mass was moving inward supersonically at the onset of star formation, whereupon  $\dot{m}_*$  spiked. According to their Figure 3a, the peak mass inflow rate was  $9.3 c_s^3/G$ , measured at  $r/r_b = 0.047$ . The infall rate dropped by half in a time of interval of  $0.62 t_{\text{ff}}$ .

For comparison, our peak accretion rate, measured much closer to the cloud center ( $r/r_b = 0.0026$ ), was  $22 c_s^3/G$ , and fell by half  $7.5 \times 10^3 \text{ yr}$  after  $t_*$ , corresponding to  $0.10 t_{\text{ff}}$ . Note that both decay times are very brief compared to the free-fall time based on the cloud’s *mean* initial density, which is  $1.7 \times 10^5 \text{ yr}$ . Any estimate of the average mass accretion rate building up the protostar based on the latter definition of  $t_{\text{ff}}$  would be grossly inadequate.

The accretion spike is also not an artefact of the spherical geometry imposed by us and other authors. Gong & Ostriker (2011) simulated in three dimensions the collapse of a plane-parallel slab built up by supersonic, converging flows. Dense condensations appeared within the postshock structure, and their evolution was qualitatively the same as those created through spherical inflow (Gong & Ostriker 2009). In particular, the authors reported a rapid rise in each core’s central density once the structure became self-gravitating, and a concurrent buildup of inward, supersonic motion. Although they could not follow the evolution past the point of star formation, the preceding

dynamical evolution leaves no doubt that  $\dot{m}_*$  would again have started out relatively high.

### 4.3. Quasi-Static Evolution

In summary, an accretion spike occurs whenever a self-gravitating cloud evolves to the point of inward collapse, regardless of the detailed initial or boundary conditions. Both the buildup of supersonic velocities throughout the bulk of the cloud and the consequent accretion spike are sharply at odds with observations. Together, observation and theory are forcing us to conclude that *low-mass star formation is a quasi-static process*. The parent cloud contracts slowly, even after it develops a large density contrast. Supersonic velocities naturally do appear after the star forms. The infall region surrounding the star subsequently spreads outward, but again in a slow, subsonic manner.

No purely hydrodynamic model, including ours, has yielded this outcome. Some other force, in addition to the thermal pressure gradient, must be resisting self-gravity and preventing a more prompt and global collapse. Perhaps the protostellar wind, which eventually disperses the entire cloud, helps to impede infall at earlier times. If so, the detailed mechanism is far from clear (see Wilkin & Stahler 1998, 2003, for studies of the wind-infall interaction). The effective pressure associated with turbulence is not a candidate, as the nonthermal velocities inside dense cores are subsonic (Barranco & Goodman 1998). We are left to reconsider the core’s magnetic field.

According to Crutcher (2012), the mass to flux ratio in dense cores, both starred and starless, is supercritical (see his Fig. 7). That is, the actual cloud mass,  $M_{\text{cl}}$ , exceeds  $M_\phi$ , the magnetic critical value:

$$M_{\text{cl}} > M_\phi \equiv \frac{1}{2\pi} \frac{\Phi}{G^{1/2}}, \quad (3)$$

where  $\Phi$  is the magnetic flux threading the cloud. Here, we have followed Crutcher (2012) and used the expression for  $M_\phi$  from Nakano & Nakamura (1978). Since starless cores are quasi-statically evolving prior to collapse,  $M_{\text{cl}}$  must still be less than the *total* critical mass, which includes also the thermal component, i.e., the Jeans mass (Stahler & Palla 2004, Section 9.4).

Over the relatively long, pre-collapse epoch, there is indeed time for ambipolar diffusion to act, especially in the core’s densest, central region. The most detailed numerical simulations of this process have focused, for simplicity, on thin-disk models of dense cores. In the still widely cited work of (Ciolek & Mouschovias 1994), the authors found that the central number density doubles in less than 1 Myr, once it has already reached values exceeding a few  $10^4 \text{ cm}^{-3}$  (see their Fig. 1). Naturally, the theoretical models are greatly oversimplified, not only in their assumption of a thin-disk geometry, but in their neglect of external turbulence and accretion. The gap between theory and observation is highlighted by the observations of Crutcher, Hakobian, & Troland (2009), who find that the mass loading of field lines in the envelopes surrounding four dense cores exceeds that in their interiors, contrary to conventional wisdom.

Current three-dimensional simulations of cloud collapse and star formation neglect any prehistory of quasi-static settling. Instead, they typically start with a cloud threaded by a uniform and relatively weak field. Under these circumstances, the cloud collapses promptly and drags in flux as it forms the star. While this alleviates the discrepancy with observations just cited, it also leads to strong magnetic braking that prevents disk formation (e.g. Krasnopolsky et al. 2012). The next frontier in theory is more careful modeling of magnetized dense cores that undergo subsonic accretion as they contract, leading to the formation of a central star under more quiescent conditions than previously envisioned.

We thank the referee for numerous comments that helped improve the final manuscript. This project was carried out while M. M. was a Visiting Scientist in the Berkeley Astronomy Department. She warmly thanks the Department for their hospitality during this productive, six-month period. S. S. was partially supported by NSF Grant 0908573.

## REFERENCES

- Aikawa, Y., Herbst, E., Roberts, H., & Caselli, P. 2005, *ApJ*, 620, 330
- Alves, J. F., Lombardi, M., & Lada, C. J. 2007, *A&A*, 462, L17
- Arzoumian, D. et al. 2011, *Å*, 529,L6
- Barranco, J. A. & Goodman, A. A. *ApJ*, 504, 207
- Belloche, A., André, P., Despois, D., & Blinder, S. 2002, *A&A*, 393, 927
- Boss, A. P. & Black, D. C. 1982, *ApJ*, 258, 270
- Choi, M., Evans, N. J., Gregersen, E. W., & Wang, Y. 1995, *ApJ*, 448, 742
- Ciolek, G. E. & Mouschovias, T. C., 1994, *ApJ*, 454, 194
- Crutcher, R. M. 2012, *ARA&A*, 50, 29
- Crutcher, R. M., Hakobian, N., & Troland, T. H. 2009, *ApJ*, 692, 844
- Dalba, P. A. & Stahler, S. W. 2012, *MNRAS*, 425, 1591
- Di Francesco, J., Myers, P. C., Wilner, D. J., Ohashi, N., & Mardones, D. 2001, *ApJ*, 562, 770
- Fatuzzo, M. & Adams, F. C. 2002, *ApJ*, 570, 210
- Forbrich, J., Lada, C., Muench, A. A., Alves, J., & Lombardi, M. 2009 *ApJ*, 704, 292
- Foster, P. N. & Chevalier, R. A. 1993, *ApJ*, 416, 30
- Gong, H. & Ostriker, E. C. 2009, *ApJ*, 699, 230
- Gong, H. & Ostriker, E. C. 2011, *ApJ*, 729, 120
- Goodman, A. A., Barranco, J. A., Wilner, D. J., & Heyer, M. H. 1998, *ApJ*, 505, 223
- Gregersen, E. M., Evans, N. J., Zhou, S., & Choi, M. 1997, *ApJ*, 484, 256
- Gregersen, E. M. & Evans, N. J. 2000, *ApJ*, 538, 260
- Hayes, J. C., Norman, M. L., Fiedler, R. A., Bordner, J. O., Li, P. S., Clark, S. E., ud-Doula, A., & MacLow M.-M. 2006, *ApJS*, 165, 188
- Hunter, C. 1977, *ApJ*, 218, 834
- Jessop, N. E. & Ward-Thompson, D. 2000, *MNRAS*, 311, 63
- Jijina, J., Myers, P. C., & Adams, F. 1999, *ApJS*, 125, 161



- Kenyon, S. J., Hartmann, L. W., Strom, K. M., & Strom, S. E. 1990, *AJ*, 99, 869
- Keto, E. & Caselli, P. 2008, *ApJ*, 683, 238
- Krasnopolsky, R., Li, Z.-Y., Shang, H., & Zhao, B. 2012, *ApJ*, 757, 77
- Larson, R. B. 1969, *MNRAS*, 145, 271
- Lee, C. W. & Myers, P. C. 2011, *ApJ*, 734, 60
- Lee, C. W., Myers, P. C., & Tafalla, M. 2001, *ApJS*, 136, 703
- Molinari, S. et al. 2010, *A*, 518, L100
- Motoyama, K. & Yoshida, T. 2003, *MNRAS*, 344, 461
- Nakano, T. & Nakamura, T. 1978, *PASJ*, 30, 681
- Ogino, S., Tomisaka, K., & Nakamura, F. 1999, *PASJ*, 51, 637
- Palmeirim, P. et al. 2012, preprint, arXiv:1211.6360
- Penston, R. V. 1969, *MNRAS*, 144, 425
- Pineda, J. E., Goodman, A. A., Arce, H. G., Caselli, P., Foster, J. B., Myers, P. C., & Rosolowsky, E. W. 2010, *ApJ*, 712, 116
- Rathborne, J. M., Lada, C. J., Muench, A. A., Alves, J. F., Kainulainen, J., & Lombardi, M. 2009, *ApJ*, 699, 742
- Ryden, B. S. 1996, *ApJ*, 471, 822
- Shirley, Y. L., Evans, N. J., & Rawlings, J. M. C. 2002, *ApJ*, 575, 337
- Shu, F. H. 1977, *ApJ*, 214, 488
- Stahler, S. W. & Palla, F. 2004, *The Formation of Stars*, (Weinheim: Wiley-VCH)
- Stahler, S. W. & Yen, J. J. 2009, *MNRAS*, 396, 579
- Stahler, S. W. & Yen, J. J. 2010, *MNRAS*, 407, 243
- Tassis, K., Willacy, K., Yorke, H. W., & Turner, N. J. 2012, *ApJ*, 753, 29
- Vorobyov, E. I. & Basu, S. 2010, *ApJ*, 719, 1896
- Walsh, A. J., Bourke, T. L., & Myers, P. C. 2003, *ApJ*, 637, 860
- Whitworth, A. & Summers, D. 1985, *MNRAS*, 214, 1

Wilkin, F. P. & Stahler, S. W. 1998, ApJ, 502, 661

Wilkin, F. P. & Stahler, S. W. 2003, ApJ, 590, 917

Collapse Simulations						
$\rho_c/\rho_b$	$t_s$ ( $10^5$ yr)	$t_*$ ( $10^5$ yr)	$t_f$ ( $10^5$ yr)	$\dot{m}_{\text{ext}}$ ( $c_s^3/G$ )	$\langle \dot{m}_* \rangle$ ( $c_s^3/G$ )	$(\dot{r}_s)_0$ ( $c_s$ )
1.00 (closed)	2.86	2.89	3.10	0.00	8.35	3.80
1.00 (open)	1.64	1.86	2.08	0.84	10.9	1.99
1.45	15.4	15.5	15.7	0.35	10.1	4.03
2.00	8.55	8.62	8.82	0.52	10.7	3.54
4.00	4.31	4.39	4.59	0.66	11.2	3.46
8.00	3.02	3.11	3.30	0.64	11.4	3.48
14.0	2.52	2.59	2.79	0.59	11.2	3.56
20.0	2.28	2.35	2.56	0.55	10.8	3.70
40.0	1.92	1.98	2.19	0.48	9.95	3.82
100	1.53	1.57	1.81	0.40	8.20	4.07

Table 1: Parameters and selected results of the simulations. From left to right, the columns are: center-to-edge density contrast of the starting state; time when the peak contraction speed becomes supersonic; time when the protostar forms; time when the protostar attains 0.3 times the current cloud mass; externally imposed mass accretion rate; average mass accretion rate onto the protostar from  $t_*$  to  $t_f$ ; outward speed of the sonic point at time  $t_*$ .

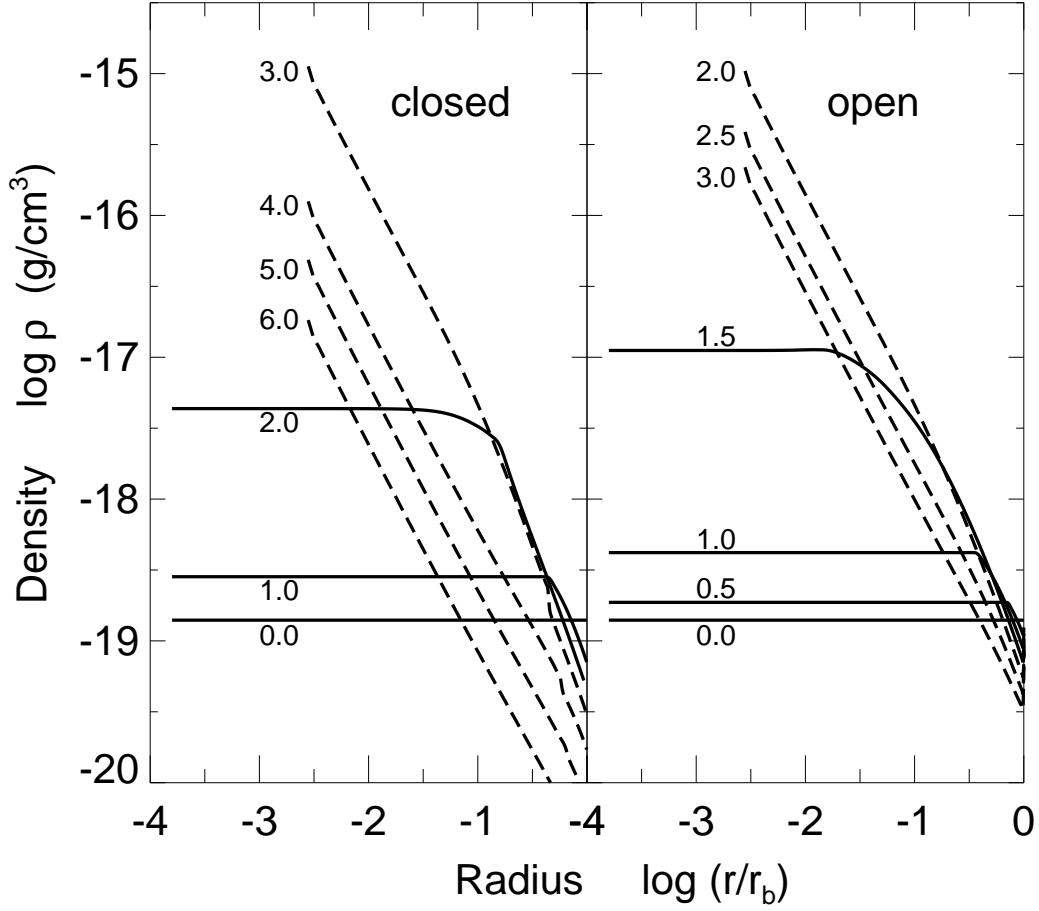


Fig. 1.— Evolution of the cloud density profile for uniform-density starting states. Left and right panels show the results for the closed and open boundary conditions, respectively. In both cases, the dashed curves are the profiles after the protostar forms. All curves are labeled by the time, in units of  $10^5$  yr.

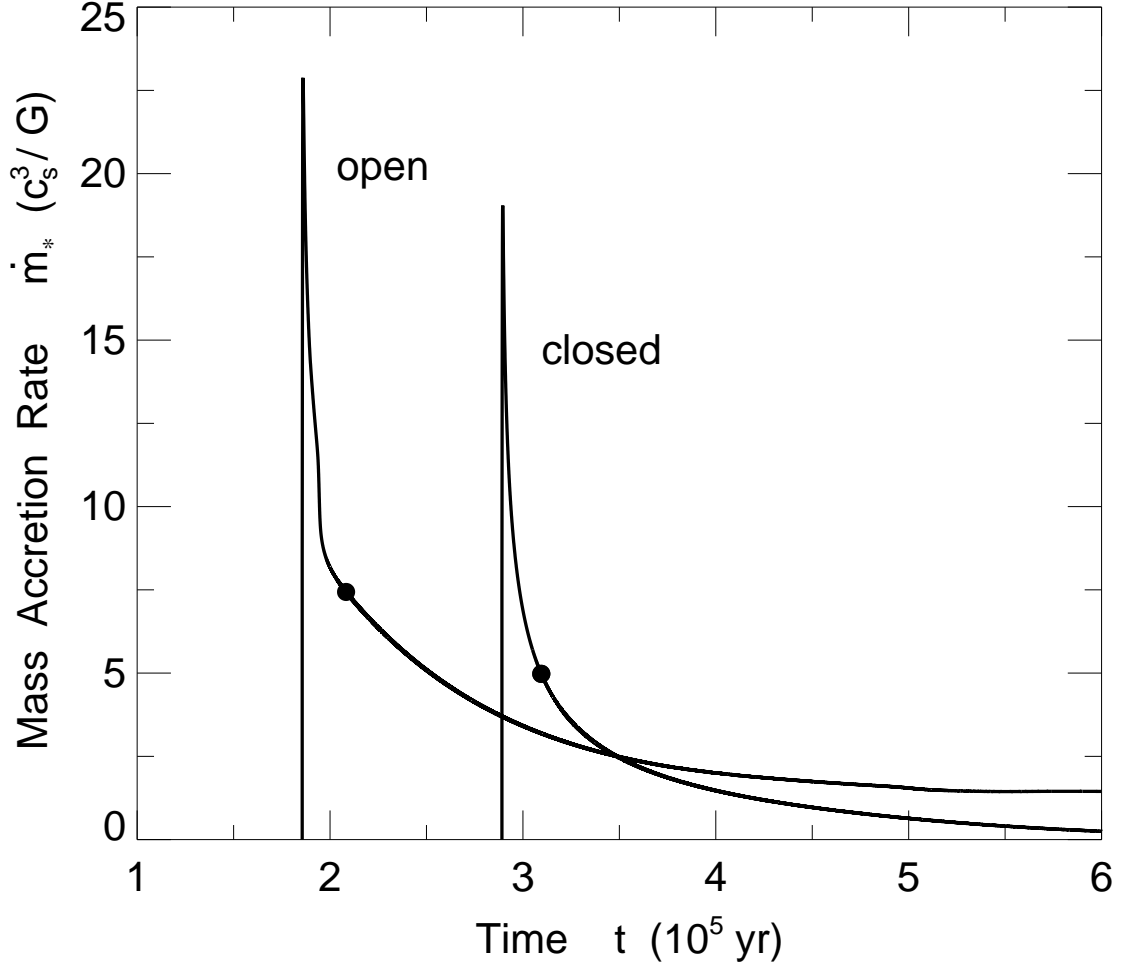


Fig. 2.— Evolution of the mass accretion rate onto the protostar, for both simulations using uniform-density starting states. The rate is shown in units of  $c_s^3/G$ . The filled circles on both curves mark the time  $t_f$ , when the central star attains its full mass.

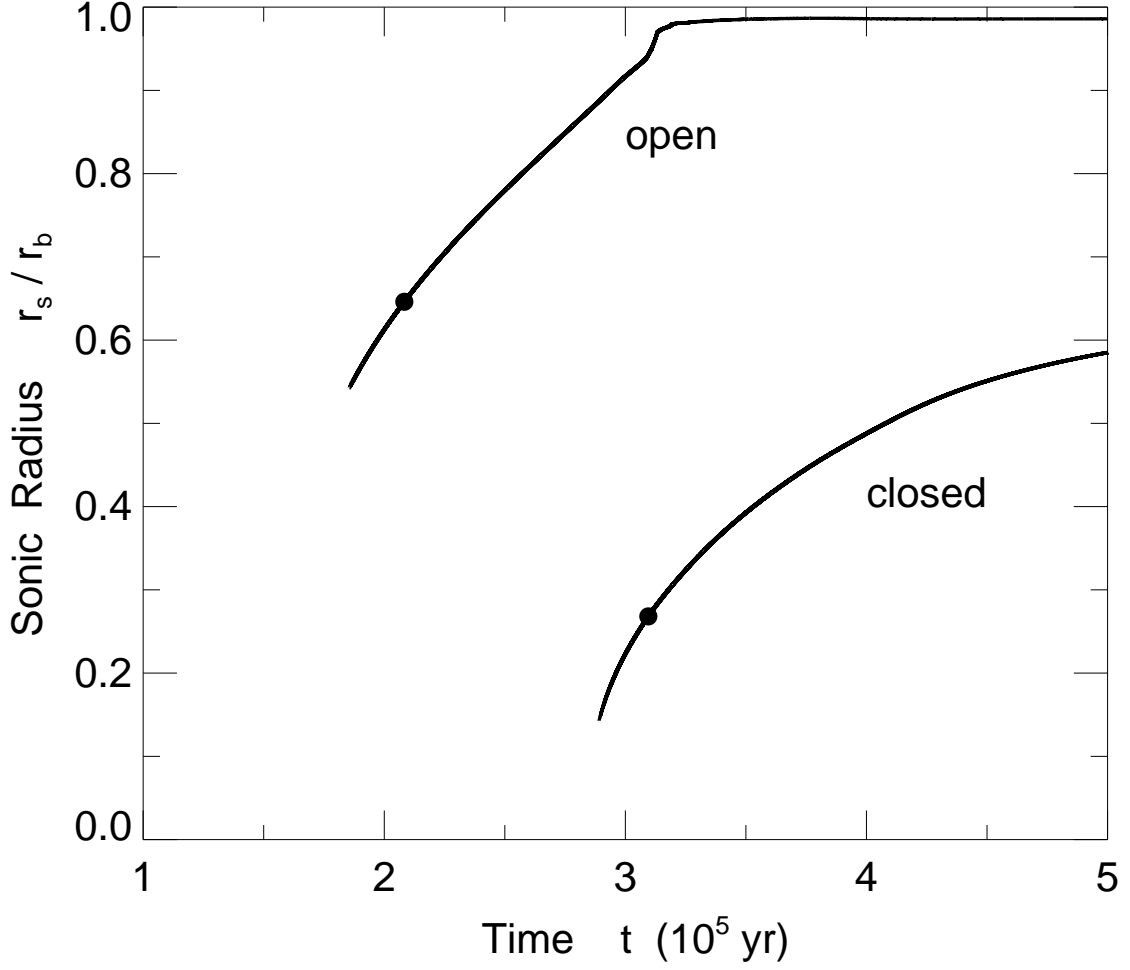


Fig. 3.— Expansion of the sonic radius, for the simulations using uniform-density starting states. Plotted is the sonic radius  $r_s$  relative to the cloud boundary  $r_b$ . The closed circles again mark the time  $t_f$ .

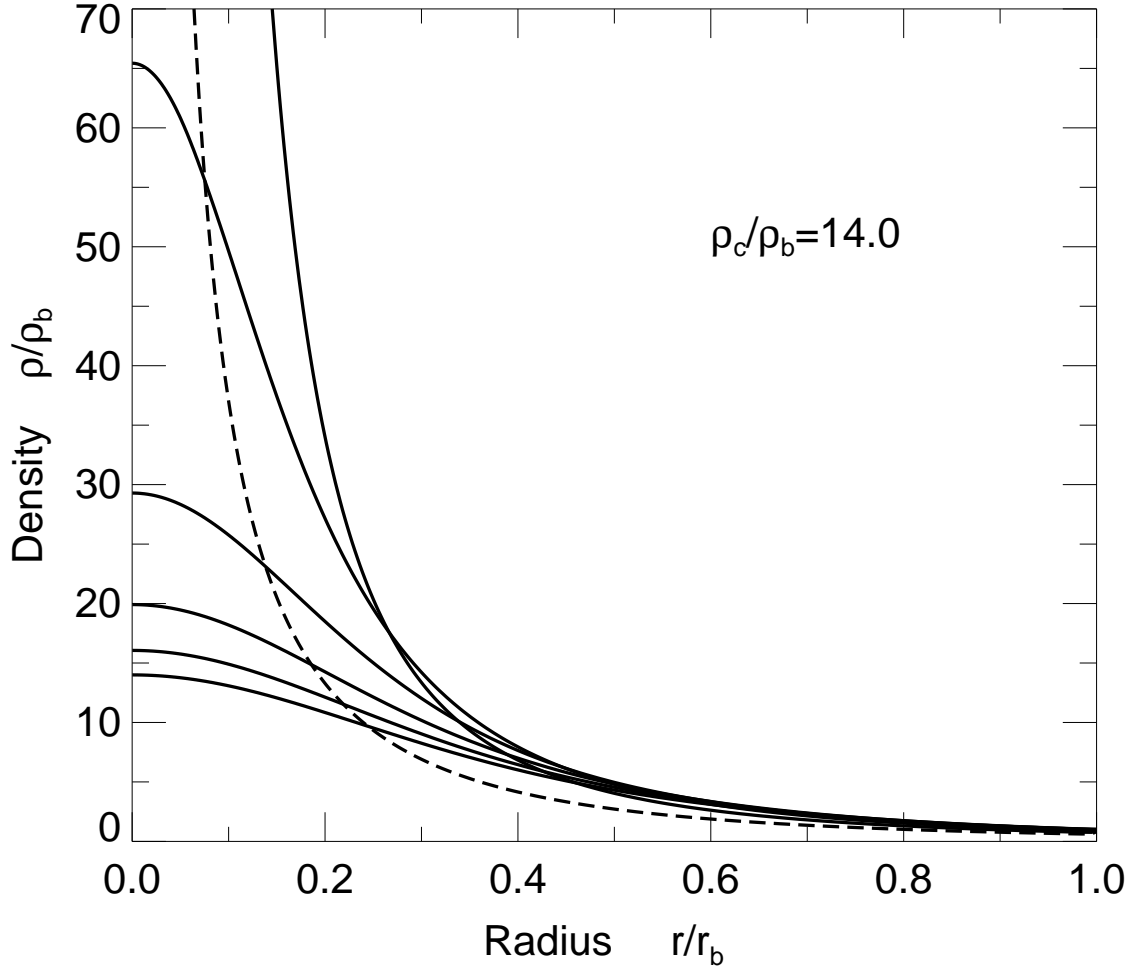


Fig. 4.— Evolution of the cloud density profile for a starting state with a center-to-edge density contrast of 14.0. The central density climbs monotonically with time. The solid curve with the lowest central density represents  $t = 0$ , and successive profiles are separated by  $\Delta t = 5 \times 10^4$  yr. The dashed curve corresponds to the latest time,  $t = 3.0 \times 10^5$  yr, which is after the point of star formation.

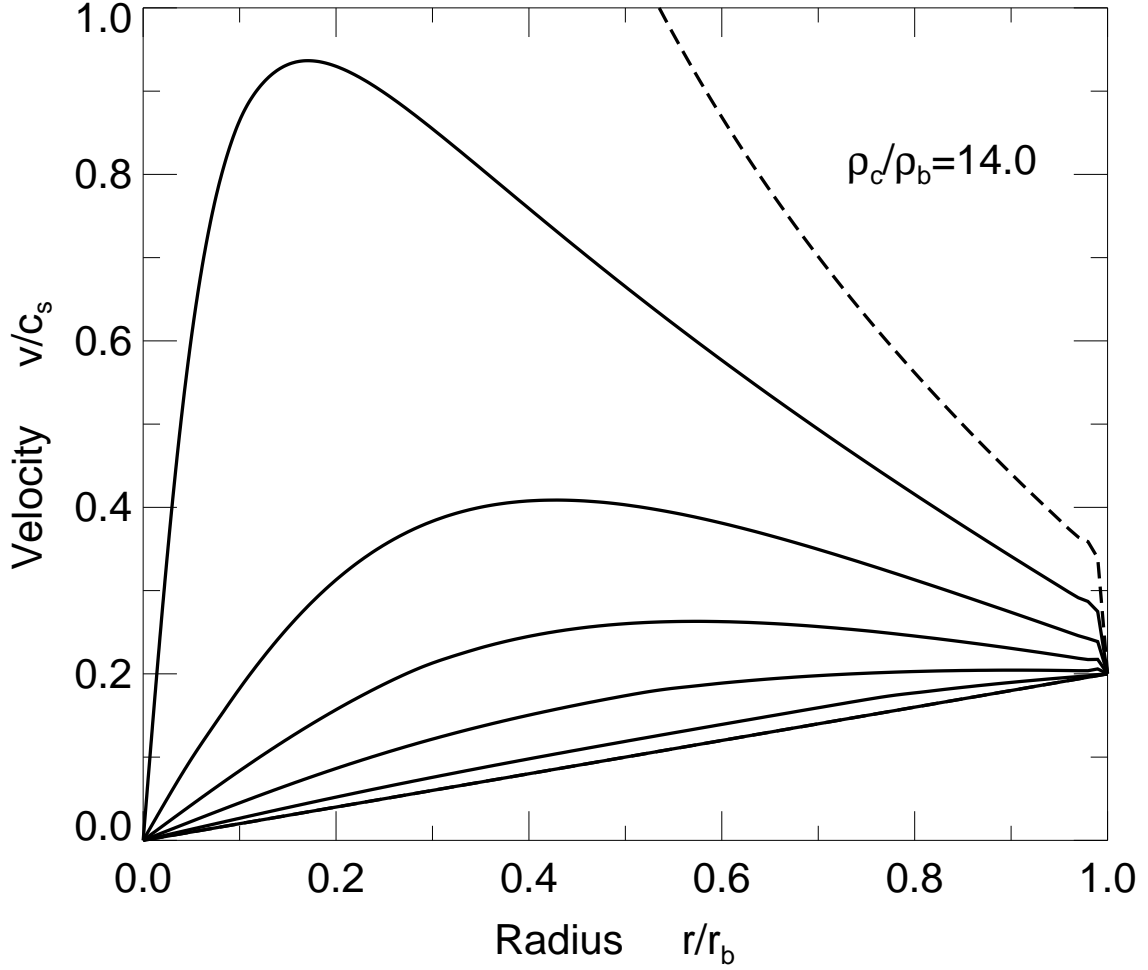


Fig. 5.— Evolution of the velocity profile for the starting state with  $\rho_c/\rho_b = 14.0$ . From bottom to top, each curve represents the same temporal sequence as in Figure 4. Again, the dashed curve is the only velocity profile after the star forms. Notice, in all profiles, the jump in velocity just inside the outer boundary.



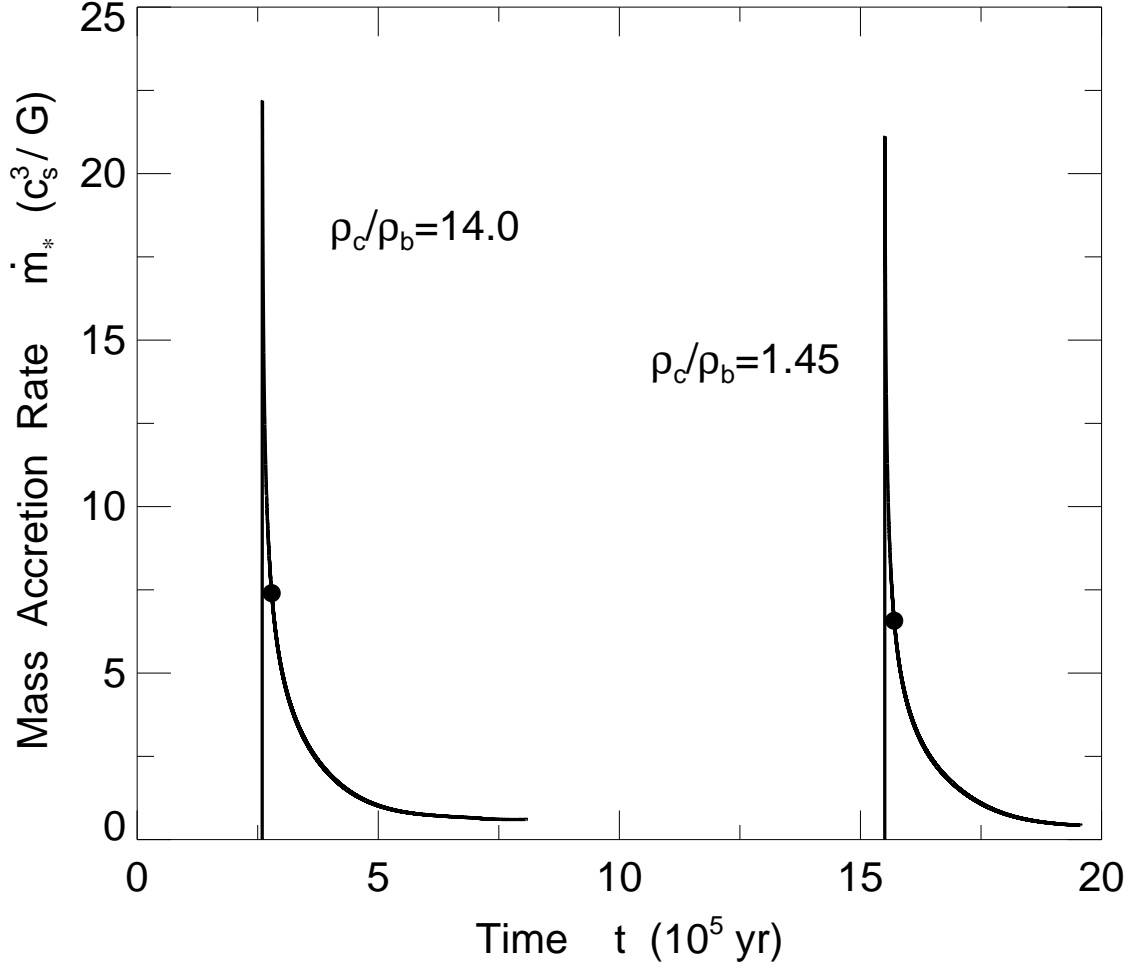


Fig. 6.— Evolution of the stellar mass accretion rate. The two starting states are both nearly in hydrostatic equilibrium, with the indicated density contrasts. The filled circles again mark the time  $t_f$ .

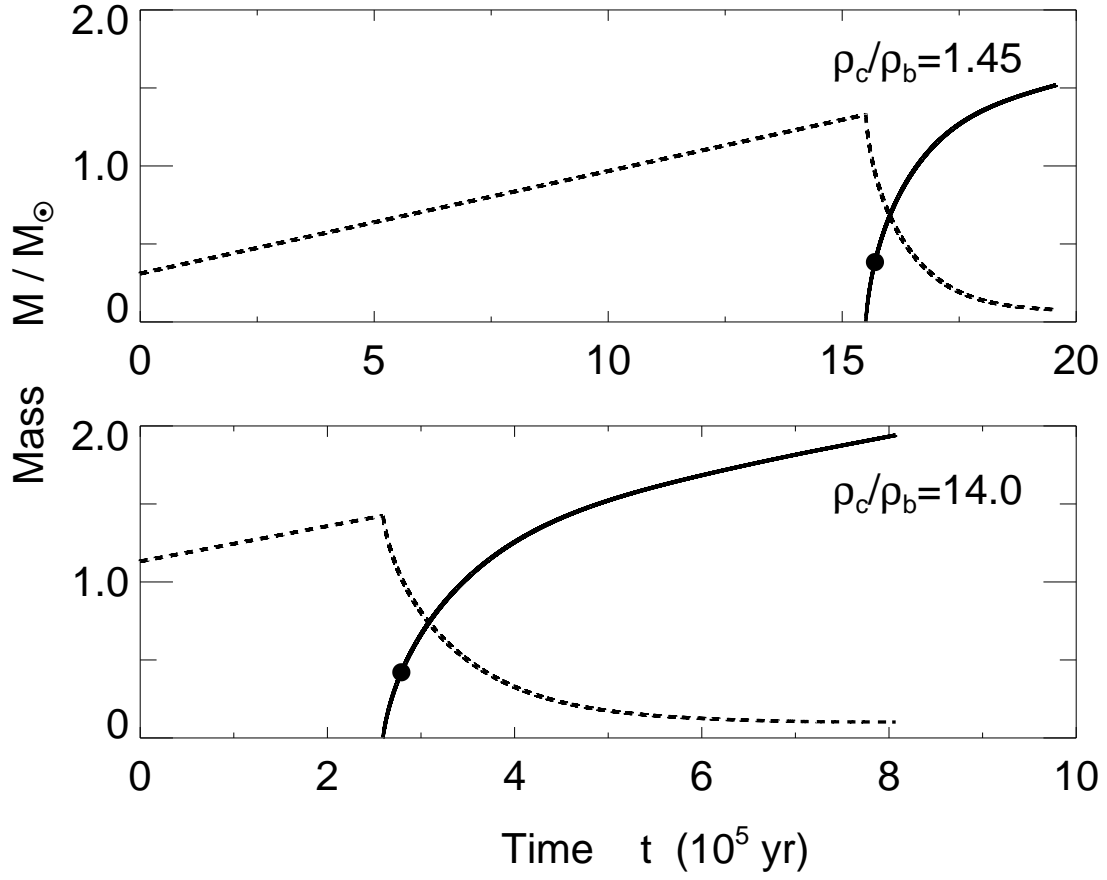


Fig. 7.— Evolution of the stellar mass (*solid curve*) and the mass of the dense core (*dashed curve*). The starting density contrast of the cloud is given in each panel. The filled circles again mark the time  $t_f$ .

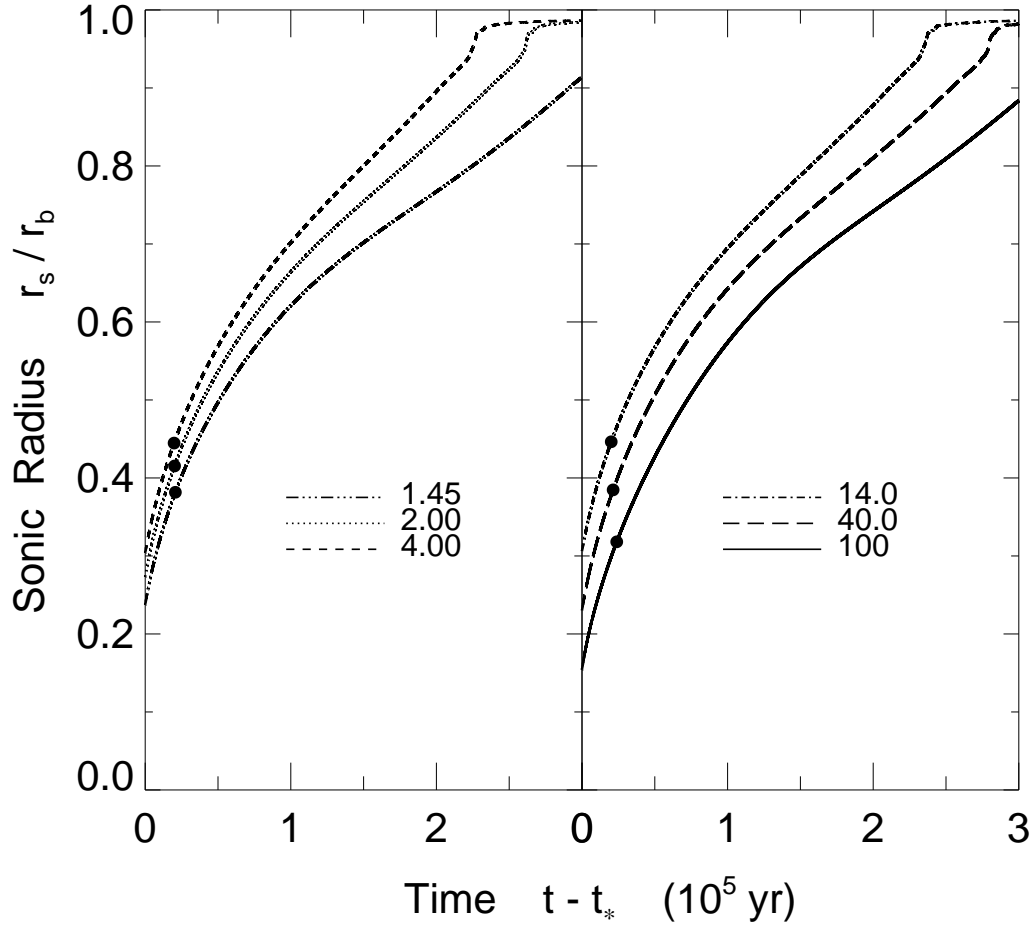


Fig. 8.— Expansion of the sonic point. Plotted is the position of  $r_s$ , normalized to the boundary radius  $r_b$ , as a function of time elapsed since star formation. Each curve corresponds to the initial density contrast indicated. The filled circles mark the time  $t_f$

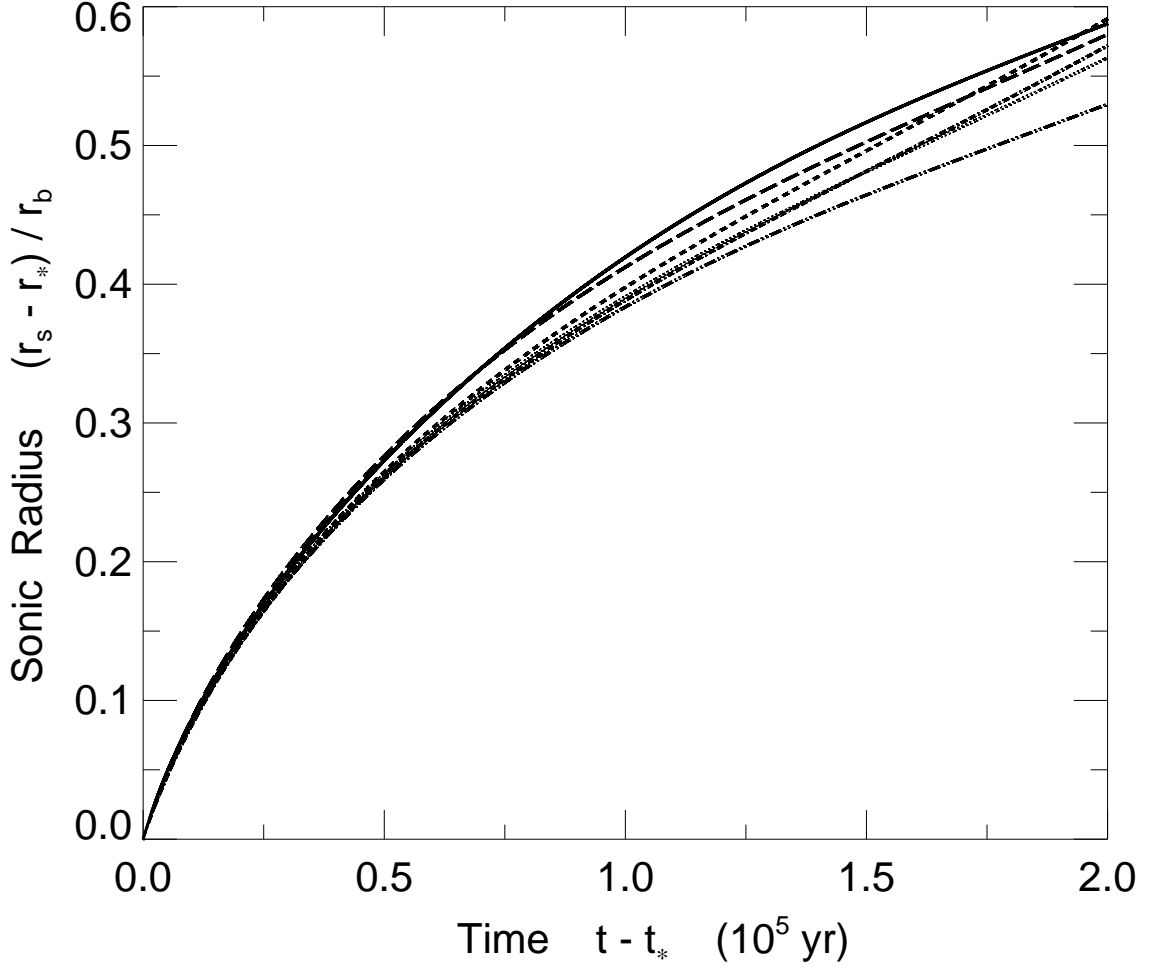


Fig. 9.— Trajectory shapes for the sonic point. Displayed are all the curves of  $r_s(t)$  from Figure 8, but renormalized to that they begin at the same location. The trajectories are remarkably similar, despite the wide range of initial cloud density contrasts.

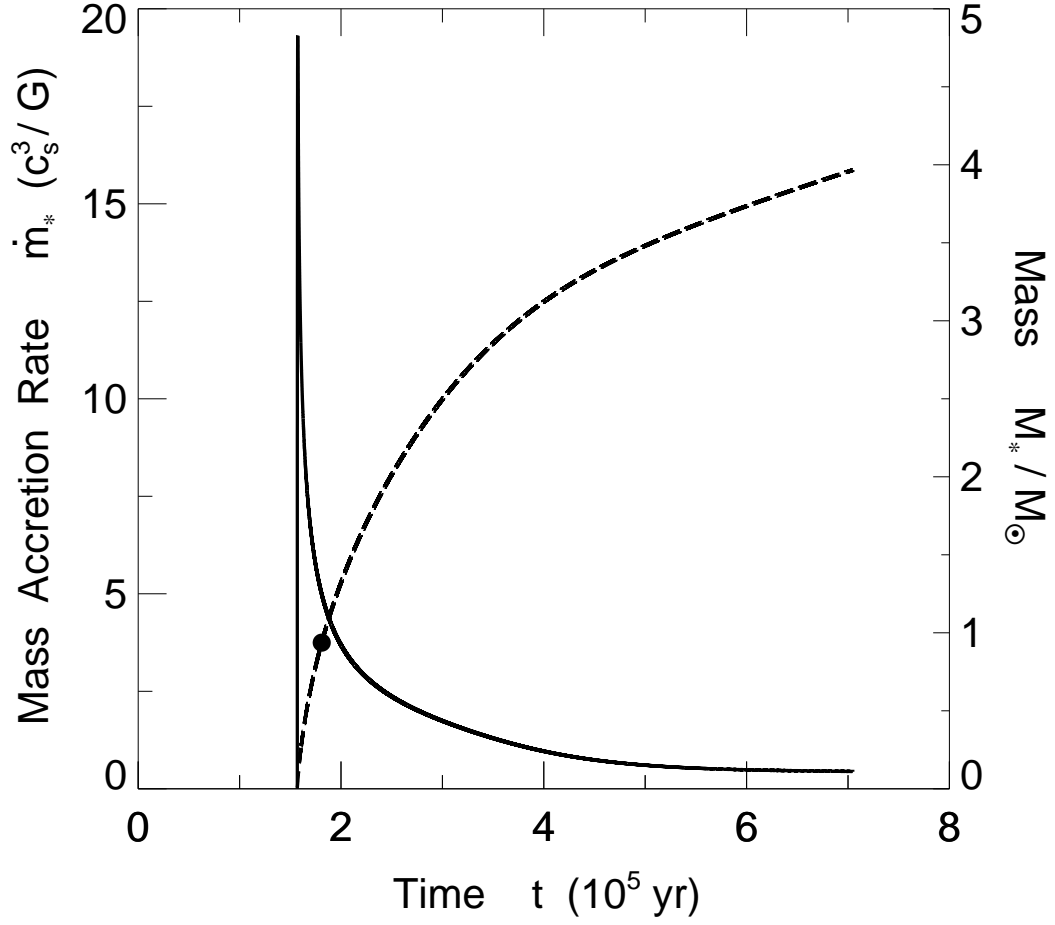


Fig. 10.— Evolution of the mass accretion rate (*solid curve*) and stellar mass (*dashed curve*) for the cloud with an initial density contrast of  $\rho_c/\rho_b = 100$ . The filled circle marks the time  $t_f$ .